Appl. Math. Mech. -Engl. Ed., **42**(3), 331–346 (2021)

APPLIED MATHEMATICS AND MECHANICS (ENGLISH EDITION)

https://doi.org/10.1007/s10483-021-2687-7

Nanoparticle aggregation effects on radiative heat transport of nanoliquid over a vertical cylinder with sensitivity analysis*

B. MAHANTHESH†, K. THRIVENI

Department of Mathematics, CHRIST (Deemed to be University),
Bangalore 560029, Karnataka, India

(Received Jul. 11, 2020 / Revised Sept. 28, 2020)

Abstract A sensitivity analysis is performed to analyze the effects of the nanoparticle (NP) aggregation and thermal radiation on heat transport of the nanoliquids (titania based on ethylene glycol) over a vertical cylinder. The optimization of heat transfer rate and friction factor is performed for NP volume fraction ($1\% \leqslant \phi \leqslant 3\%$), radiation parameter ($1 \leqslant R_{\mathrm{t}} \leqslant 3$), and mixed convection parameter ($1.5 \leqslant \lambda \leqslant 2.5$) via the face-centered central composite design (CCD) and the response surface methodology (RSM). The modified Krieger and Dougherty model (MKDM) for dynamic viscosity and the Bruggeman model (BM) for thermal conductivity are utilized to simulate nanoliquids with the NP aggregation aspect. The complicated nonlinear problem is treated numerically. It is found that the temperature of nanoliquid is enhanced due to the aggregation of NPs. The friction factor is more sensitive to the volume fraction of NPs than the thermal radiation and the mixed convection parameter. Furthermore, the heat transport rate is more sensitive to the effect of radiative heat compared with the NP volume fraction and mixed convection parameter.

Key words nanoparticle (NP) aggregation, nanoliquid, surface heat flux, response surface methodology (RSM), sensitivity analysis

Chinese Library Classification O302
2010 Mathematics Subject Classification 34B15, 62K20, 76D99

1 Introduction

The heating and cooling of functioning fluids play an important role in the mechanical, electrical, power, and manufacturing industries. The high energy systems have to be cooled by utilizing the effective cooling technique. In this view, employing common coolants like ethylene glycol, water, oils, and propylene glycol are not satisfactory because of their poor thermal efficiency. One way of improving the thermal property of common coolant is by suspending nano-sized particles (such as Cu, Ni, Ag, Au, TiO_2,CuO, Al_2O_3, and ZnO) into the base fluid. Here the amalgamation of coolant and nanoparticles (NPs) is termed as nanoliquid, which can fade the excess of heat due to higher thermal conductivity (see Choi and Eastman[1]).

* Citation: MAHANTHESH, B. and THRIVENI, K. Nanoparticle aggregation effects on radiative heat transport of nanoliquid over a vertical cylinder with sensitivity analysis. *Applied Mathematics and Mechanics* (*English Edition*), **42**(3), 331–346 (2021) https://doi.org/10.1007/s10483-021-2687-7
† Corresponding author, E-mail: mahanthesh.b@christuniversity.in

The three-dimensional (3D) convective transport of TiO_2-ethylene glycol nanoliquid over an extending plate was investigated by Hosseinzadeh at al.[2]. They proved that the heat flux and the amount of NPs are directly proportional. The magneto-nanofluid transport past an extendable disk subjected to a space-related heat source was examined by Mahanthesh et al.[3]. They established that the heat transport rate is more influenced by the thermophoresis feature in comparison with haphazard motion. Mebarek-Oudina[4] studied the natural convective flow of TiO_2 with various base fluids in a cylindrical annulus. The nanoliquid transport on a permeable extending/shrinking cylinder was addressed by Roşca et al.[5]. They found that there exists a single and twin solution for extending plate and shrinking plate cases respectively.

Besides, experimental studies[6–7] proved that nanoliquids have higher thermal conductivity than conventional coolants due to the haphazard motion and aggregation of NP having a percolation nature. Combining particles/molecules in a specific pattern to form a long structure with strong bonding is referred to as aggregation. The relative viscosity of the aggregated particles and thermophysical properties of NPs are modeled using the fractal theory. Ellahi et al.[8] analyzed the influence of NP aggregation on the wedge flow of Al_2O_3-H_2O nanoliquid. They proved that the fractal dimensions and temperature profiles are inversely proportional. The magneto-natural convective flow of CNT-H_2O nanoliquid using the NP aggregation was investigated by Benos et al.[9]. This study showed that the nanoliquids exhibit diverse rheological properties depending on the formation of aggregation. Acharya et al.[10] examined the NP aggregation on nanoliquid inside a revolving channel. Their results proved that the heat transport rate decays for the radius of the gyration factor at the lower plate but it enhances at the upper plate.

On the other hand, the heat transmission due to thermal radiation has a major role in nuclear plants, gas turbines, space vehicles, aircraft missiles, and satellites. The mixed convective transport in an extending cylinder was investigated by Mukhopadhyay and Ishak[11]. They found a higher heat transport rate and friction factor on the boundary in the case of the cylinder than a flat plate. Mahanthesh et al.[12] examined the radiative flow of nanofluid over a nonlinearly extended plate subjected to prescribed surface heat flux. They showed that the heat transport rate enhances due to the thermal radiation aspect. The behavior of radiation aspect on mixed convective transport over an inclined cylinder subjected to deviating heat cause/drop was inspected by Hayat et al.[13]. Their study showed that heat transport rises with the curvature parameter. Pandey and Kumar[14] investigated the natural convective transport of nanoliquid past an extending permeable cylinder. Their results proved that the friction factor reduces with the radiation aspect. The magneto-nanoliquid flow in a squeezing channel subject to thermal radiation was inspected by Shit and Mukherjee[15]. However, theoretical investigations studying the effect of aggregation in a cylinder in the presence of radiative heat were extremely limited.

The thermal enhancement due to TiO_2 NPs, NP aggregation, and radiative heat on the transport of ethylene glycol-based TiO_2 nanoliquid past a vertical cylinder having surface heat flux have been analyzed for the first time. The heat transfer rate and friction factor are optimized via the response surface methodology (RSM) and central composite design (CCD). The numerical solution for nonlinear equations is obtained via a finite difference method (FDM). Comprehensive interpretations are made through the graphical and tabular forms.

2 Mathematical formulation

Consider a steady, two-dimensional, and laminar flow of an incompressible nanoliquid (TiO_2-ethylene glycol) in a semi-infinite vertical cylinder with radius a. A cylindrical coordinate system is chosen in such a way that the x-axis is along the axial direction (along with acceleration due to gravity but in the reverse direction), and the r-axis is perpendicular to the cylinder (see Fig. 1). The modified Krieger and Dougherty model (MKDM) for viscosity and Bruggeman

model (BM) for thermal conductivity are utilized to simulate nanoliquids with NP aggregation. Further, the prescribed surface heat flux ($q_{\mathrm{w}}(x)$) at the surface and thermal radiation aspects are also taken into account. Let free stream velocity $U(x) = \frac{c_1 x}{l}$ flow over the cylinder, where c_1 is a positive constant, and l is the characteristic length. An ambient temperature of the fluid is denoted by T_∞. The effect of viscous dissipation and slip velocity between the base liquid and NPs is neglected. The governing expressions are listed as follows (see Refs. [16]–[17]).

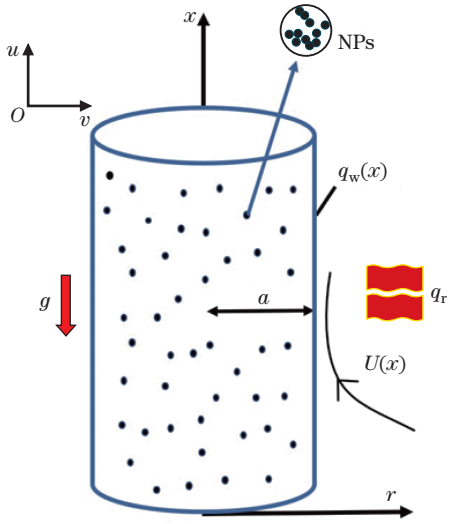

Fig. 1 Sketch of physical model (color online)

The continuity equation is

$$\frac{\partial}{\partial x}(ru) + \frac{\partial}{\partial r}(rv) = 0, \tag{1}$$

the linear momentum equation is

$$\rho_{\mathrm{nf}}\Big(u\frac{\partial u}{\partial x} + v\frac{\partial u}{\partial r}\Big) = \rho_{\mathrm{nf}} U\frac{\mathrm{d}U}{\mathrm{d}x} + \mu_{\mathrm{nf}}\Big(\frac{\partial^2 u}{\partial r^2} + \frac{1}{r}\frac{\partial u}{\partial r}\Big) + g(\rho\beta_0)_{\mathrm{nf}}(T - T_\infty), \tag{2}$$

the energy equation is

$$(\rho c_p)_{\mathrm{nf}}\Big(u\frac{\partial T}{\partial r} + v\frac{\partial T}{\partial r}\Big) = k_{\mathrm{nf}}\Big(\frac{\partial^2 T}{\partial r^2} + \frac{1}{r}\frac{\partial T}{\partial r}\Big) - \frac{1}{r}\frac{\partial}{\partial r}(rq_{\mathrm{r}}), \tag{3}$$

accounting Rosseland approximation for optically thick media, q_{r} is given by[13]

$$q_{\mathrm{r}} = -\frac{4\sigma^*}{3k^*}\Big(\frac{\partial T^4}{\partial r}\Big), \tag{4}$$

expanding T^4 about T_∞ by using the Taylor series and neglecting higher-order terms give

$$T^4 \cong 4T_\infty^3 T - 3T_\infty^4, \tag{5}$$

and plugging Eqs. (4)–(5) into Eq. (3) yields

$$(\rho c_p)_{\mathrm{nf}}\Big(u\frac{\partial T}{\partial r} + v\frac{\partial T}{\partial r}\Big) = \Big(k_{\mathrm{nf}} + \frac{16\sigma^* T_\infty^3}{3k^*}\Big)\frac{1}{r}\frac{\mathrm{d}}{\mathrm{d}r}\Big(r\frac{\mathrm{d}T}{\mathrm{d}r}\Big), \tag{6}$$

where u and v are velocities, and T, g, q_{r}, σ^*, and k^* correspond to the temperature, acceleration due to gravity, radiative heat flux, Stefan-Boltzmann constant, and mean absorption coefficient, respectively. μ, ρ, β_0, c_p, and k are, respectively, referring to viscosity, density, coefficient of thermal expansion, heat capacitance, and thermal conductivity. The subscripts 'nf' and 'f' represent the nanoliquid and base liquid, respectively.

The associate boundary conditions are (see Refs. [16]–[17])

$$\begin{cases} u = 0, \quad v = 0, \quad k_{\mathrm{nf}} \dfrac{\partial T}{\partial r} = -q_{\mathrm{w}}(x) \quad \text{at} \quad r = a, \\ u \to U_{\mathrm{w}}(x) = \dfrac{c_1 x}{l}, \quad T \to T_\infty \quad \text{as} \quad r \to \infty. \end{cases} \tag{7}$$

From the experimental data, it is well known that the nanoliquids have remarkable thermal conductivity. Further, an enhancement in the thermal property can be achieved by haphazard motion of NPs or due to NP aggregation causing percolation behavior. The Brownian randomness decays compared with aggregation which boosts the mass of aggregates, whereas the percolation behavior of aggregates can lead to an enhancement of thermal conductivity. Owing to this, on redefining the thermophysical properties of nanofluid for NP aggregation, the effective viscosity (μ_{nf}), density (ρ_{nf}), thermal expansion coefficient ($(\beta_0)_{\mathrm{nf}}$), heat capacitance ($(c_p)_{\mathrm{nf}}$), and thermal conductivity (k_{nf}) are listed as follows (see Refs. [6]–[8])

$$\begin{aligned} \mu_{\mathrm{nf}} &= \mu_{\mathrm{f}} \Big(1 - \frac{\phi_{\mathrm{agg}}}{\phi_{\max}}\Big)^{-2.5\phi_{\max}}, \\ \rho_{\mathrm{nf}} &= (1 - \phi_{\mathrm{agg}})\rho_{\mathrm{f}} + (\phi\rho)_{\mathrm{agg}}, \\ (\rho\beta_0)_{\mathrm{nf}} &= (1 - \phi_{\mathrm{agg}})(\rho\beta_0)_{\mathrm{f}} + \phi_{\mathrm{agg}}(\rho\beta_0)_{\mathrm{agg}}, \\ (\rho c_p)_{\mathrm{nf}} &= (1 - \phi_{\mathrm{agg}})(\rho c_p)_{\mathrm{f}} + \phi_{\mathrm{agg}}(\rho c_p)_{\mathrm{agg}}, \\ k_{\mathrm{nf}} &= k_{\mathrm{f}} \Big(\frac{k_{\mathrm{agg}} + 2k_{\mathrm{f}} + 2\phi_{\mathrm{agg}}(k_{\mathrm{agg}} - k_{\mathrm{f}})}{k_{\mathrm{agg}} + 2k_{\mathrm{f}} - \phi_{\mathrm{agg}}(k_{\mathrm{agg}} - k_{\mathrm{f}})}\Big), \end{aligned}$$

where the correlations for μ_{nf} and k_{nf} are taken from the MKDM and the modified Maxwell model, respectively. The thermal characteristics of particles aggregation (denoted by subscript 'agg') are given by (see Refs. [6]–[8])

$$\begin{aligned} &\rho_{\mathrm{agg}} = (1 - \phi_{\mathrm{int}})\rho_{\mathrm{f}} + \phi_{\mathrm{int}}\rho_{\mathrm{s}}, \quad \phi_{\mathrm{agg}} = \frac{\phi}{\phi_{\mathrm{int}}}, \quad \phi_{\mathrm{int}} = \Big(\frac{R_{\mathrm{agg}}}{R_{\mathrm{p}}}\Big)^{D-3}, \\ &(\rho\beta_0)_{\mathrm{agg}} = (1 - \phi_{\mathrm{int}})(\rho\beta_0)_{\mathrm{f}} + \phi_{\mathrm{int}}(\rho\beta_0)_{\mathrm{s}}, \\ &(\rho c_p)_{\mathrm{agg}} = (1 - \phi_{\mathrm{int}})(\rho c_p)_{\mathrm{f}} + \phi_{\mathrm{int}}(\rho c_p)_{\mathrm{s}}, \\ &k_{\mathrm{agg}} = \frac{k_{\mathrm{f}}}{4}\Big((3\phi_{\mathrm{int}} - 1)\frac{k_{\mathrm{s}}}{k_{\mathrm{f}}} + (3(1 - \phi_{\mathrm{int}}) - 1) + \Big(\Big((3\phi_{\mathrm{int}} - 1)\frac{k_{\mathrm{s}}}{k_{\mathrm{f}}} \\ &\qquad + (3(1 - \phi_{\mathrm{int}}) - 1)\Big)^2 + \frac{8k_{\mathrm{s}}}{k_{\mathrm{f}}}\Big)^{\frac{1}{2}}\Big), \end{aligned}$$

where k_{agg} is a value of the BM for spherical particles. Here, ϕ, ϕ_{agg}, ϕ_{int}, and $\phi_{\max}$ are the NP volume fraction, the effective particle volume fraction of aggregates, NP volume fraction within the aggregate, and maximum particle packing fraction ($\phi_{\max} = 0.605$ for particles of spherical shape), respectively. From the fractal theory, R_{agg} and R_{p} correspond to radii of aggregates and primary NPs (the value of $\frac{R_{\mathrm{agg}}}{R_{\mathrm{p}}}$ is taken as 3.34). D is the fractal index, in general for spherical particles which takes the value 1.8. The effective thermal conductivity of TiO_2-ethylene glycol nanoliquid can be predicted accurately by utilizing the Maxwell and BM which is more realistic. The similarity solutions to Eqs. (1), (2), and (6) can be obtained by

utilizing the appropriate transformation as follows[16–17]:

$$\begin{cases} \eta = \dfrac{r^2 - a^2}{2a}\Big(\dfrac{U_{\rm w}}{\nu_{\rm f} x}\Big)^{\frac{1}{2}}, \quad \Psi(x,r) = a(U_{\rm w}\nu_{\rm f} x)^{\frac{1}{2}} f(\eta), \quad U_{\rm w}(x) = \dfrac{c_1 x}{l}, \\ q_{\rm w}(x) = \dfrac{c_2 x}{l}, \quad T = T_\infty + \dfrac{q_{\rm w}}{k_{\rm f}}\Big(\dfrac{\nu_{\rm f} x}{U_{\rm w}}\Big)^{\frac{1}{2}}\theta(\eta), \quad u = \dfrac{1}{r}\dfrac{\partial \Psi}{\partial r}, \quad v = -\dfrac{1}{r}\dfrac{\partial \Psi}{\partial r}. \end{cases} \tag{8}$$

Here, η and Ψ correspond to similarity variable and stream function, respectively. c_2 is a positive constant. Using Eq. (8) and thermophysical properties of nanoliquid for aggregation approach, Eq. (1) satisfies trivially, and Eqs. (2), (6), and (7) take the following forms:

$$(2\eta\gamma + 1)f'''(\eta) + 2\gamma f''(\eta) + \frac{A_2}{A_1}(1 + f(\eta)f''(\eta) - (f'(\eta))^2) + \lambda\frac{A_3}{A_1}\theta(\eta) = 0, \tag{9}$$

$$\Big(1 + \frac{4R_{\rm t}}{3A_5}\Big)((2\eta\gamma + 1)\theta''(\eta) + 2\gamma\theta'(\eta)) + \frac{A_4}{A_5}Pr(f(\eta)\theta'(\eta) - f'(\eta)\theta(\eta)) = 0, \tag{10}$$

$$\begin{cases} f'(\eta) = 0, \quad f(\eta) = 0, \quad A_5\theta'(\eta) = -1 \quad \text{at} \quad \eta = 0, \\ f'(\eta) \to 1, \quad \theta(\eta) \to 0 \quad \text{as} \quad \eta \to \infty, \end{cases} \tag{11}$$

where

$$\begin{aligned} A_1 &= \Big(1 - \frac{\phi_{\rm agg}}{\phi_{\max}}\Big)^{-2.5\phi_{\max}}, \\ A_2 &= (1 - \phi_{\rm agg}) + \phi_{\rm agg}\frac{\rho_{\rm agg}}{\rho_{\rm f}}, \\ A_3 &= (1 - \phi_{\rm agg}) + \phi_{\rm agg}\frac{(\rho\beta_0)_{\rm agg}}{(\rho\beta_0)_{\rm f}}, \\ A_4 &= (1 - \phi_{\rm agg}) + \phi_{\rm agg}\frac{(\rho c_p)_{\rm agg}}{(\rho c_p)_{\rm f}}, \\ A_5 &= \frac{k_{\rm agg} + 2k_{\rm f} + 2\phi_{\rm agg}(k_{\rm agg} - k_{\rm f})}{k_{\rm agg} + 2k_{\rm f} - \phi_{\rm agg}(k_{\rm agg} - k_{\rm f})}. \end{aligned}$$

The dimensionless parameters in Eqs. (9) and (10) are defined as follows:

$$\begin{aligned} \gamma &= \frac{1}{a}\Big(\frac{\nu_{\rm f} l}{c_1}\Big)^{\frac{1}{2}}, \\ \lambda &= \frac{Gr}{Re^{\frac{5}{2}}} = \frac{g(\beta_0)_{\rm f} c_2 l^{(3/2)}\nu_{\rm f}^{\frac{1}{2}}}{k_{\rm f} c_1^{5/2}}, \\ Gr &= \frac{g\beta_0 c_2 l^4}{k_{\rm f}\nu_{\rm f}^2}, \quad Re = (c_1 l)/\nu_{\rm f}, \\ Pr &= \frac{\nu_{\rm f}(\rho c_p)_{\rm f}}{k_{\rm f}}, \quad R_{\rm t} = \frac{4\sigma^* T_\infty^3}{k^* k_{\rm f}}, \end{aligned}$$

where γ is the curvature parameter, λ is the mixed convection parameter, Gr is the Grashof number, Re is the Reynolds number, Pr is the Prandtl number, and $R_{\rm t}$ is the thermal radiation parameter. The expressions for the skin friction coefficient ($S_{\rm F}$) and local Nusselt number (Nu_x) are given by (see Ref. [19])

$$\frac{1}{2}Re_x^{0.5} S_{{\rm F}x} = A_1 f''(0), \quad Re_x^{-0.5} Nu_x = A_5\frac{1}{\theta(0)}, \tag{12}$$

where $Re_x = \frac{c_1 x^2}{l\nu_{\rm f}}$ (the local Reynolds number).

3 Solution methodology

Linear differential equations (9)–(10) with Eq. (11) are solved by using the bvp4c routine in MATLAB. This routine is based on the FDM. Equations (9)–(10) are first converted into a system of the single-order differential system by substituting $f = y_1$, $f' = y_2$, $f'' = y_3$, $\theta = y_4$, and $\theta' = y_5$ as follows:

$$\begin{cases} y_1' = y_2, \\ y_2' = y_3, \\ y_3' = \dfrac{1}{(2\eta\gamma + 1)}\Big(- \dfrac{A_3}{A_1}\lambda y_4 - 2\gamma y_3 - \dfrac{A_2}{A_1}(1 + y_1 y_3 - y_2^2)\Big), \\ y_4' = y_5, \\ y_5' = \dfrac{1}{(2\eta\gamma + 1)}\Big(- 2\gamma y_5 - \dfrac{A_4}{A_5} Pr(y_1 y_5 - y_2 y_4)\Big(1 + \dfrac{4R_{\mathrm{t}}}{3A_5}\Big)^{-1}\Big) \end{cases} \tag{13}$$

with the corresponding initial conditions

$$y_1(0) = y_2(0) = 0, \quad y_3(0) = 1, \quad y_4(0) = t, \quad y_5(0) = -\frac{1}{A_5}, \tag{14}$$

where the initial guess is denoted by t. A comparison of $f''(0)$ and $\frac{1}{\theta(0)}$ with the previously published data is made when $\lambda = 1$, $\gamma = 0$, $R_{\mathrm{t}} = 0$, and $\phi = 0$ to validate the method employed (see Table 1). From Table 1, the comparison shows favorable agreement.

Table 1 Values of $f''(0)$ and $1/\theta(0)$ for diverse values of Pr when $\lambda = 1$, $\gamma = 0$, $R_{\mathrm{t}} = 0$, and $\phi = 0$

Pr	Ramachandran et al.[18]		Ishak[17]		Present result	
	$f''(0)$	$1/\theta(0)$	$f''(0)$	$1/\theta(0)$	$f''(0)$	$1/\theta(0)$
0.7	1.833 9	0.777 6	1.833 9	0.777 6	1.833 8	0.777 6
1	–	–	1.733 8	0.878 0	1.733 8	0.878 1
7	1.403 7	1.691 2	1.403 7	1.691 2	1.403 8	1.691 3
10	–	–	1.371 2	1.906 7	1.371 1	1.906 7

4 Results and discussion

The dimensionless velocity ($f'(\eta)$) and temperature ($\theta(\eta)$) profiles are computed for diverse values of effective parameters such as thermal radiation parameter (R_{t}), curvature parameter (γ), mixed convection parameter (λ), and NP volume fraction (ϕ) versus dimension space coordinate (η), which are displayed graphically. Further, to understand the behavior of skin friction coefficient $\left(\frac{1}{2}Re_x^{0.5}S_{\mathrm{F}x}\right)$ and local Nusselt number ($Re_x^{-0.5}Nu_x$), an optimization procedure is performed through the RSM. The Prandtl number is taken as 150.45 for ethylene glycol at 300 K. Also, the values for other parameters are fixed as $\gamma = 0.2$, $\lambda = 4$, $R_{\mathrm{t}} = 2$, and $\phi = 0.03$ unless otherwise specified. Figures 2–9 are plotted for two diverse cases, namely, (i) Case I: with aggregation ($\phi_{\mathrm{int}} \neq 1$), (ii) Case II: without aggregation ($\phi_{\mathrm{int}} = 1$). The qualitative behavior of $f'(\eta)$ and $\theta(\eta)$ is the same for both cases; however, quantitatively they are different. Further, $f'(\eta)$ is found to be higher for Case II than Case I whereas the reverse trend is observed for $\theta(\eta)$.

4.1 Parametric analysis

The impact of R_{t} on $f'(\eta)$ and $\theta(\eta)$ is presented in Figs. 2–3. $f'(\eta)$ and $\theta(\eta)$ increase with an ascending value of R_{t}. Physically, this is due to the availability of excessive heat in the nanoliquid system through the radiation process; as a result, the liquid particles move faster. Figures 4–5 illustrate the behavior of $f'(\eta)$ and $\theta(\eta)$ for the numerous values of γ. $f'(\eta)$ decays for increasing values of γ whereas the opposite trend is noticed for $\theta(\eta)$. Here, $\gamma = 0$ represents the flat plate. The thermal diffusion of the nanoliquid is controlled by the coefficient $(2\gamma\eta + 1)$.

The effect of λ on $f'(\eta)$ and $\theta(\eta)$ is displayed in Figs. 6–7. $\theta(\eta)$ decreases with a rising value of λ whereas reverse nature is observed for $f'(\eta)$. This is due to stronger buoyancy force, higher values of λ imply larger buoyancy force which corresponds to the higher velocity field $f'(\eta)$ and lesser temperature field $\theta(\eta)$. The influence of ϕ on $f'(\eta)$ and $\theta(\eta)$ is illustrated in Figs. 8–9. $f'(\eta)$ and $\theta(\eta)$ are, respectively, decaying and growing with an ascending value of ϕ due to the inclusion of more NPs.

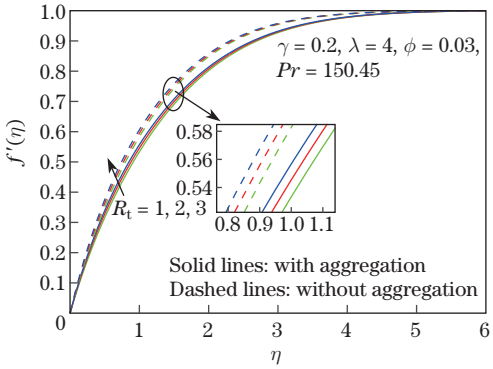

Fig. 2 Impact of R_t on $f'(\eta)$ (color online)

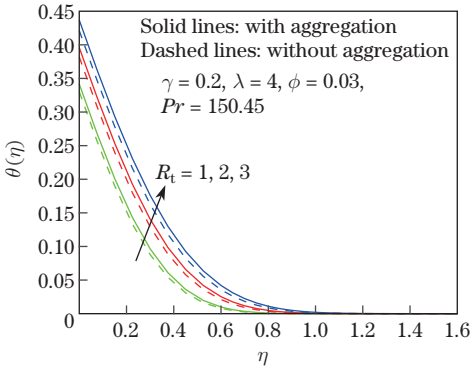

Fig. 3 Impact of R_t on $\theta(\eta)$ (color online)

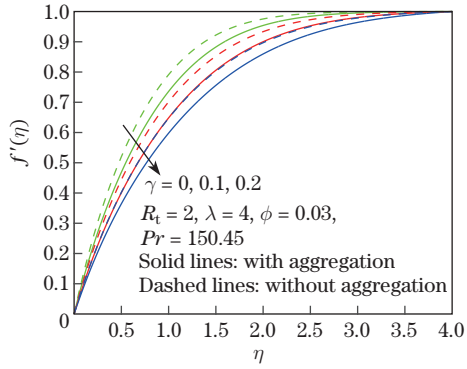

Fig. 4 Impact of γ on $f'(\eta)$ (color online)

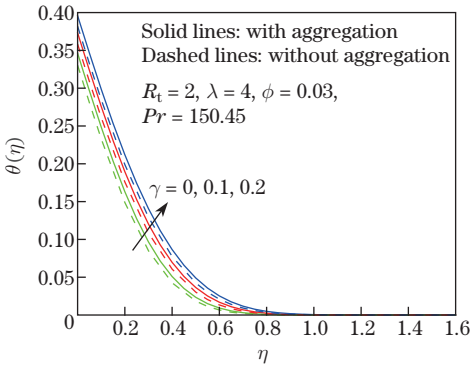

Fig. 5 Impact of γ on $\theta(\eta)$ (color online)

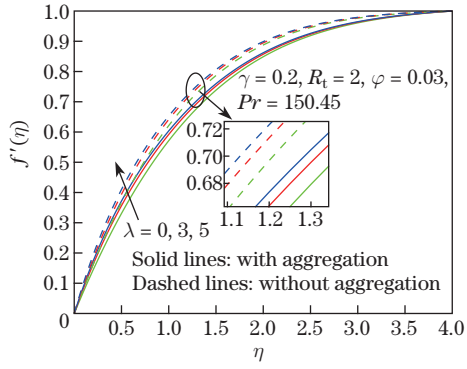

Fig. 6 Impact of λ on $f'(\eta)$ (color online)

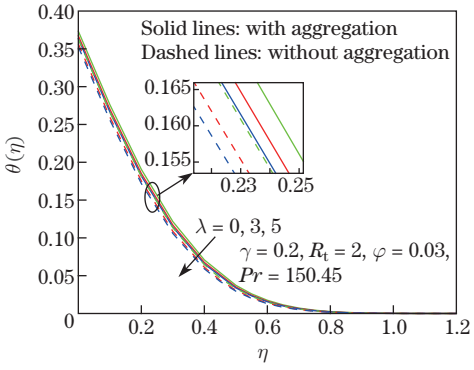

Fig. 7 Impact of λ on $\theta(\eta)$ (color online)

4.2 RSM

The relations between effective parameters (R_t, λ, ϕ) and response variables (skin friction coefficient S_F and local Nusselt number Nu_x) are well explained by a statistical approach known as the RSM. The chosen range of effective parameters and their levels based on the face-centered CCD are tabulated in Table 2. The main advantage of this model is that it includes linear,

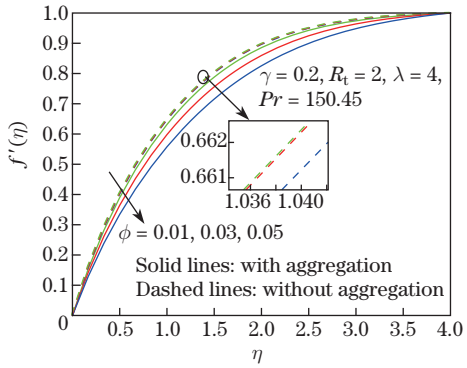

Fig. 8 Impact of ϕ on $f'(\eta)$ (color online)

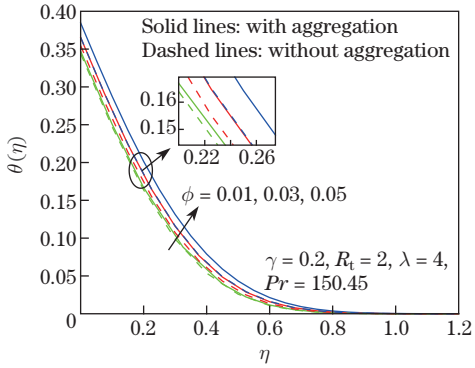

Fig. 9 Impact of ϕ on $\theta(\eta)$ (color online)

quadratic, and interaction terms. The experimental design and the responses are recorded in Table 3. The general forms of correlation of effective parameters (R_t, λ, ϕ) on response variables (S_F and Nu_x) are given as follows:

$$S_F = m_0 + m_1 R_t + m_2 \lambda + m_3 \phi + m_{11} R_t^2 + m_{22} \lambda^2 + m_{33} \phi^2 + m_{12} R_t \lambda + m_{13} R_t \phi + m_{23} \lambda \phi, \quad (15)$$

$$Nu_x = p_0 + p_1 R_t + p_2 \lambda + p_3 \phi + p_{11} R_t^2 + p_{22} \lambda^2 + p_{33} \phi^2 + p_{12} R_t \lambda + p_{13} R_t \phi + p_{23} \lambda \phi, \quad (16)$$

where m_0 and p_0 are the intercepts, m_1, m_2, m_3, p_1, p_2, and p_3 are the linear term coefficients, m_{11}, m_{22}, m_{33}, p_{11}, p_{22}, and p_{33} are the quadratic term coefficients, and m_{12}, m_{13}, m_{23}, p_{12}, p_{13}, and p_{23} are the interaction term coefficients.

Table 2 Levels of effective parameters based on CCD-RSM

Parameter	Symbol	Level		
		−1 (low)	0 (middle)	1 (high)
R_t $(1 \leqslant R_t \leqslant 3)$	W_1	1	2	3
λ $(1.5 \leqslant \lambda \leqslant 2.5)$	W_2	1.5	2	2.5
ϕ $(0.01 \leqslant \phi \leqslant 0.05)$	W_3	0.01	0.03	0.05

Table 3 Responses with their experimental design

Run	Coded value			Real value			Response variable	
	W_1	W_2	W_3	R_t	λ	ϕ	S_F	Nu_x
1	−1	−1	−1	1	1.5	0.01	1.666 547	3.610 690
2	1	−1	−1	3	1.5	0.01	1.695 000	2.822 725
3	−1	1	−1	1	2.5	0.01	1.699 242	3.628 118
4	1	1	−1	3	2.5	0.01	1.745 957	2.839 001
5	−1	−1	1	1	1.5	0.05	2.648 485	3.906 644
6	1	−1	1	3	1.5	0.05	2.684 834	3.021 828
7	−1	1	1	1	2.5	0.05	2.688 986	3.918 149
8	1	1	1	3	2.5	0.05	2.748 904	3.035 059
9	−1	0	0	1	2	0.03	2.071 927	3.768 275
10	1	0	0	3	2	0.03	2.114 608	2.930 648
11	0	−1	0	2	1.5	0.03	2.071 319	3.234 815
12	0	1	0	2	2.5	0.03	2.119 102	3.249 121
13	0	0	−1	2	2	0.01	1.703 484	3.127 020
14	0	0	1	2	2	0.05	2.695 298	3.354 429
15	0	0	0	2	2	0.03	2.095 299	3.242 008
16	0	0	0	2	2	0.03	2.095 299	3.242 008
17	0	0	0	2	2	0.03	2.095 299	3.242 008
18	0	0	0	2	2	0.03	2.095 299	3.242 008
19	0	0	0	2	2	0.03	2.095 299	3.242 008
20	0	0	0	2	2	0.03	2.095 299	3.242 008

4.2.1 Accuracy of model

The accuracy of the model is validated via the analysis of variance table and residual plots (see Table 4 and Fig. 10). The data variance and the significance of the regression model are assessed by F- and p-values. The terms in the model are said to be significant and are considered if their F-value > 1 and p-value < 0.05, otherwise they are ignored. Owing to this, the quadratic term of λ from model (a) is removed. Similarly, the quadratic terms of λ and ϕ along with the interaction terms $R_t \times \lambda$ and $\lambda \times \phi$ are neglected from model (b). Further, the better-fitted model is achieved as R^2 and adjusted R^2 tent to unity (see Table 4). The normal probability plot shows that all the data points are aligned along the straight line, and the bar chart is approximately symmetric without much skewness. This proves that the obtained data are normal. Based on these facts, the chosen model is valid, and it has a good fit. The models for S_F and Nu_x by considering only the significant regression coefficients from Table 5 give

$$S_F = 0.021\,412R_t + 0.023\,601\lambda + 0.495\,628\phi - 0.002\,041{R_t}^2 + 0.104\,082\phi^2 + 0.005\,229R_t\lambda + 0.002\,637R_t\phi + 0.002\,615\lambda\phi + 2.095\,30, \quad (17)$$

$$Nu_x = -0.418\,60R_t + 0.006\,94\lambda + 0.120\,52\phi + 0.107\,48R_t^2 - 0.023\,43R_t\phi + 3.242\,00. \quad (18)$$

Table 4 ANOVA for (a) S_F and (b) Nu_x

Source	Degree of freedom	Adjusted sum of squares	Adjusted mean squares	F-value	p-value
		Model (a)			
Model (a)	9	2.519 80	0.279 98	710 693.60	0.000
Linear	3	2.466 62	0.822 21	2 087 082.65	0.000
R_t	1	0.004 58	0.004 58	11 637.32	0.000
λ	1	0.005 57	0.005 57	14 138.51	0.000
ϕ	1	2.456 47	2.456 47	6 235 472.13	0.000
Square	3	0.052 85	0.017 62	44 719.70	0.000
R_t^2	1	0.000 01	0.000 01	29.09	0.000
λ^2	1	0.000 00	0.000 00	0.07	0.801
ϕ^2	1	0.029 79	0.029 79	75 621.67	0.000
Interaction	3	0.000 33	0.000 11	278.45	0.000
$R_t \times \lambda$	1	0.000 22	0.000 22	555.22	0.000
$R_t \times \phi$	1	0.000 06	0.000 06	141.25	0.000
$\lambda \times \phi$	1	0.000 05	0.000 05	138.87	0.000
Error	10	0.000 00	0.000 00	–	–
Lack-of-fit	5	0.000 00	0.000 00	–	–
Pure error	5	0.000 00	0.000 00	–	–
Total	19	2.519 81			
R^2=100.00%		Adjusted R^2=100.00%			
		Model (b)			
Model (b)	9	1.959 32	0.217 70	18 715.94	0.000
Linear	3	1.897 98	0.632 66	54 390.10	0.000
R_t	1	1.752 25	1.752 25	150 642.15	0.000
λ	1	0.000 48	0.000 48	41.37	0.000
ϕ	1	0.145 24	0.145 24	12 486.77	0.000
Square	3	0.056 94	0.018 98	1 631.68	0.000
R_t^2	1	0.031 77	0.031 77	2 730.90	0.000
λ^2	1	0.000 00	0.000 00	0.00	0.000
ϕ^2	1	0.000 00	0.000 00	0.38	0.000
Interaction	3	0.004 40	0.001 47	126.03	0.000
$R_t \times \lambda$	1	0.000 00	0.000 00	0.17	0.691
$R_t \times \phi$	1	0.004 39	0.004 39	377.58	0.000
$\lambda \times \phi$	1	0.000 00	0.000 00	0.34	0.575
Error	10	0.000 12	0.000 01	–	–
Lack-of-fit	5	0.000 12	0.000 02	–	–
Pure error	5	0.000 00	0.000 00	–	–
Total	19	1.959 43			
R^2=99.99%		Adjusted R^2=99.99%			

Table 5 Estimated regression coefficients for (a) S_F and (b) Nu_x

Term	Model (a)		Model (b)	
	Coefficient	p-value	Coefficient	p-value
Constant	2.095 30	0.000	3.242 00	0.000
R_t	0.021 412	0.000	−0.418 60	0.000
λ	0.023 601	0.000	0.006 94	0.000
ϕ	0.495 628	0.000	0.120 52	0.000
R_t^2	−0.002 041	0.000	0.107 48	0.000
λ^2	−0.000 098	0.801	−0.000 02	0.993
ϕ^2	0.104 082	0.000	−0.001 26	0.553
$R_t \times \lambda$	0.005 229	0.000	0.000 49	0.691
$R_t \times \phi$	0.002 637	0.000	−0.023 43	0.000
$\lambda \times \phi$	0.002 615	0.000	−0.000 70	0.575

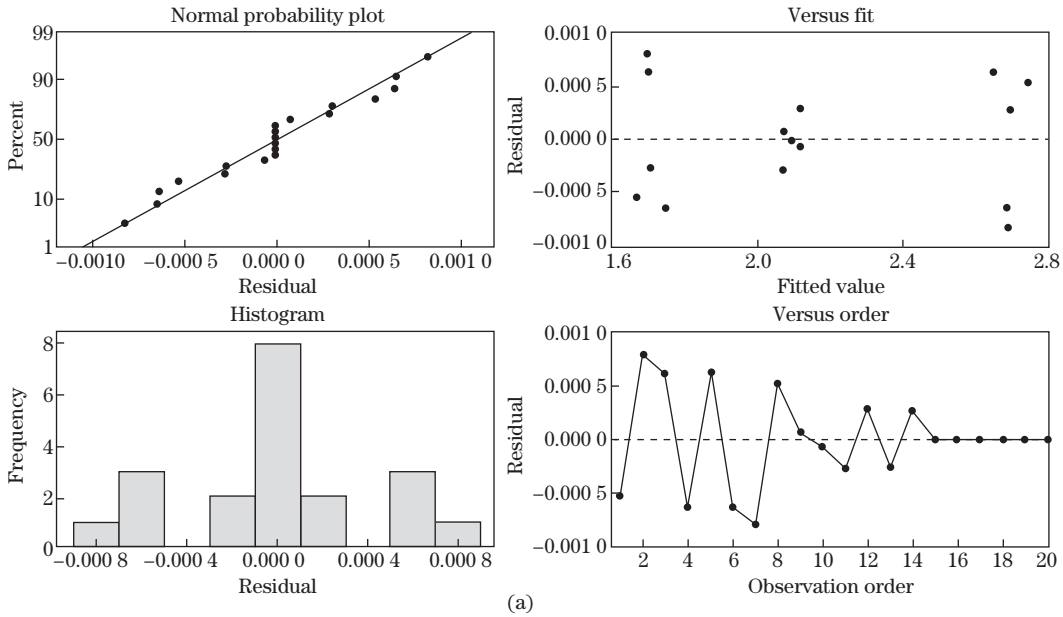

(a)

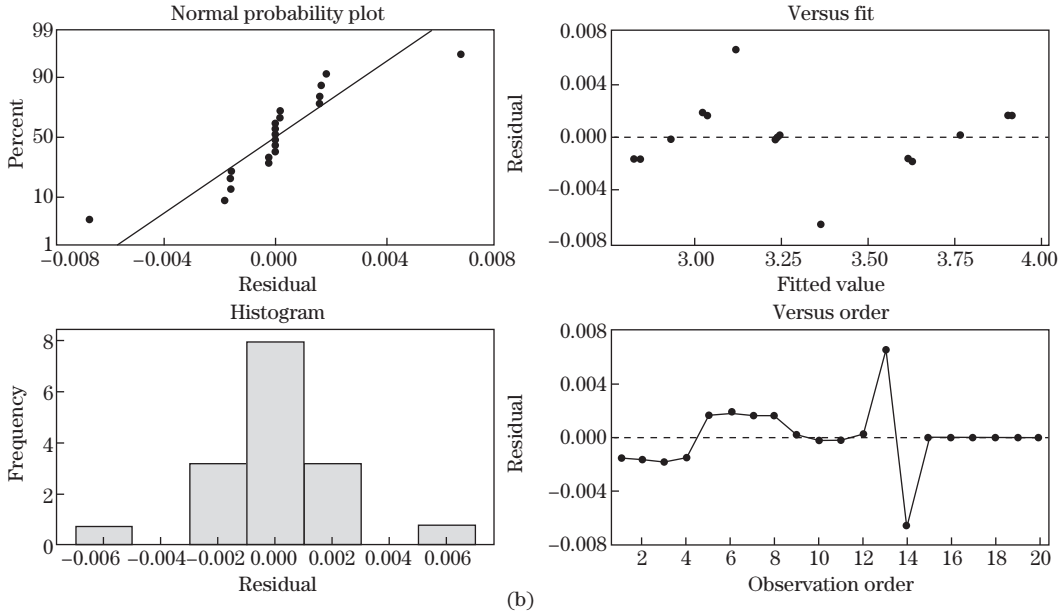

(b)

Fig. 10 Residual plots for (a) S_F and (b) Nu_x

The effects of effective parameters (R_t, λ, ϕ) on S_F and Nu_x are examined by utilizing contour and surface plots. Figures 11 and 12 are plotted to study the impact of two parameters by fixing the third parameter at the middle level. Figure 11(a) shows the impact of R_t and λ. It is analyzed that, highest level of R_t and λ correspond to the maximum value for S_F. The variation of R_t and ϕ on S_F is displayed in Fig. 11(b), and the maximum S_F is noticed at high levels of R_t and ϕ. The effect of interaction λ with ϕ is sketched in Fig. 11(c), and an enhancement in S_F is found for ascending values of λ and ϕ. Also, at the high levels of λ and ϕ maximum S_F is observed. From Fig. 12(a) a maximum Nu_x is achieved for a low level of R_t and high level of λ. Similarly, the maximum value of Nu_x is noticed for a low level of R_t and high level of ϕ (see Fig. 12(b)). Figure 12(c) portrays the influence of interaction λ with ϕ

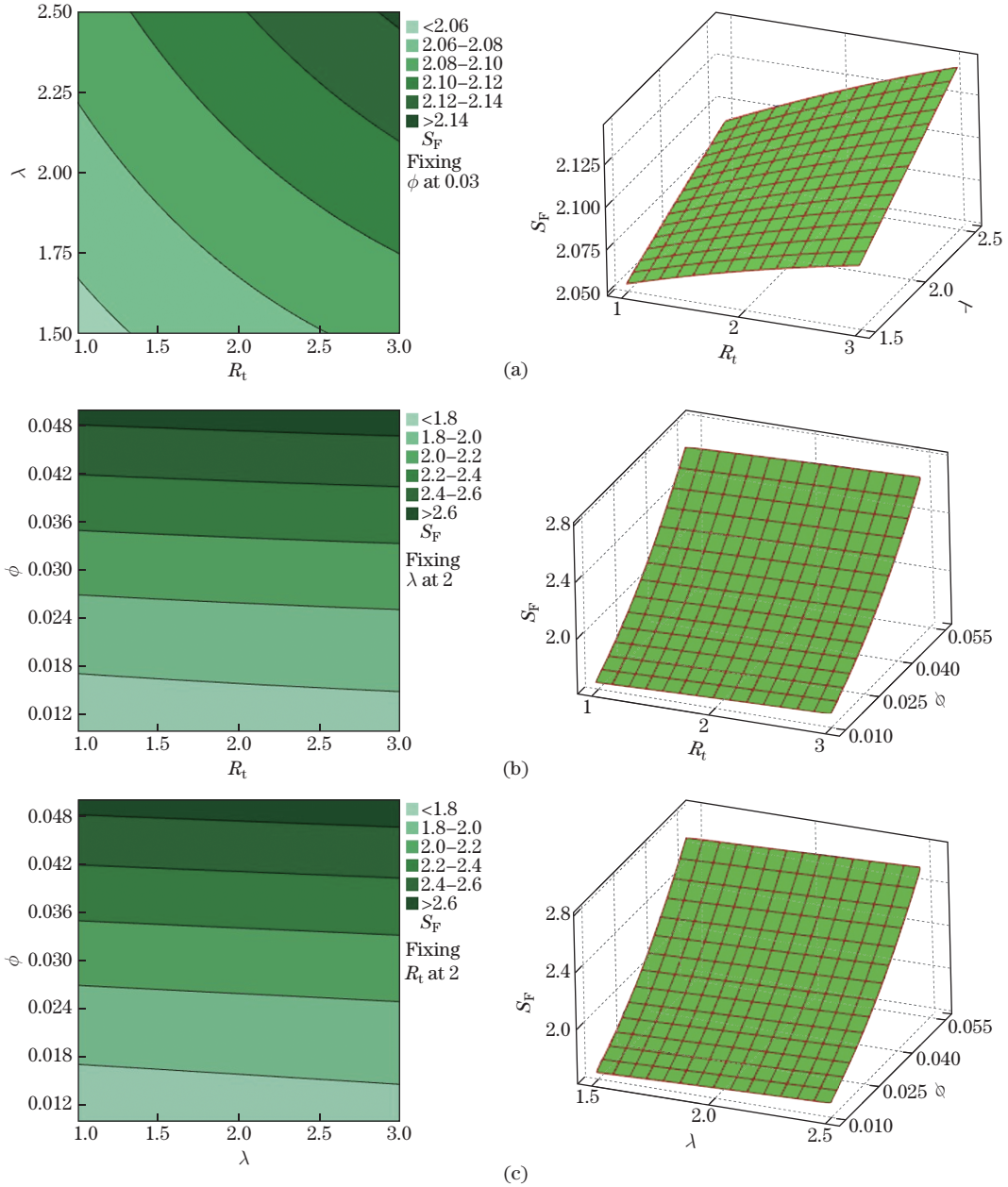

Fig. 11 Contours (left) and surface plots (right) for S_F (color online)

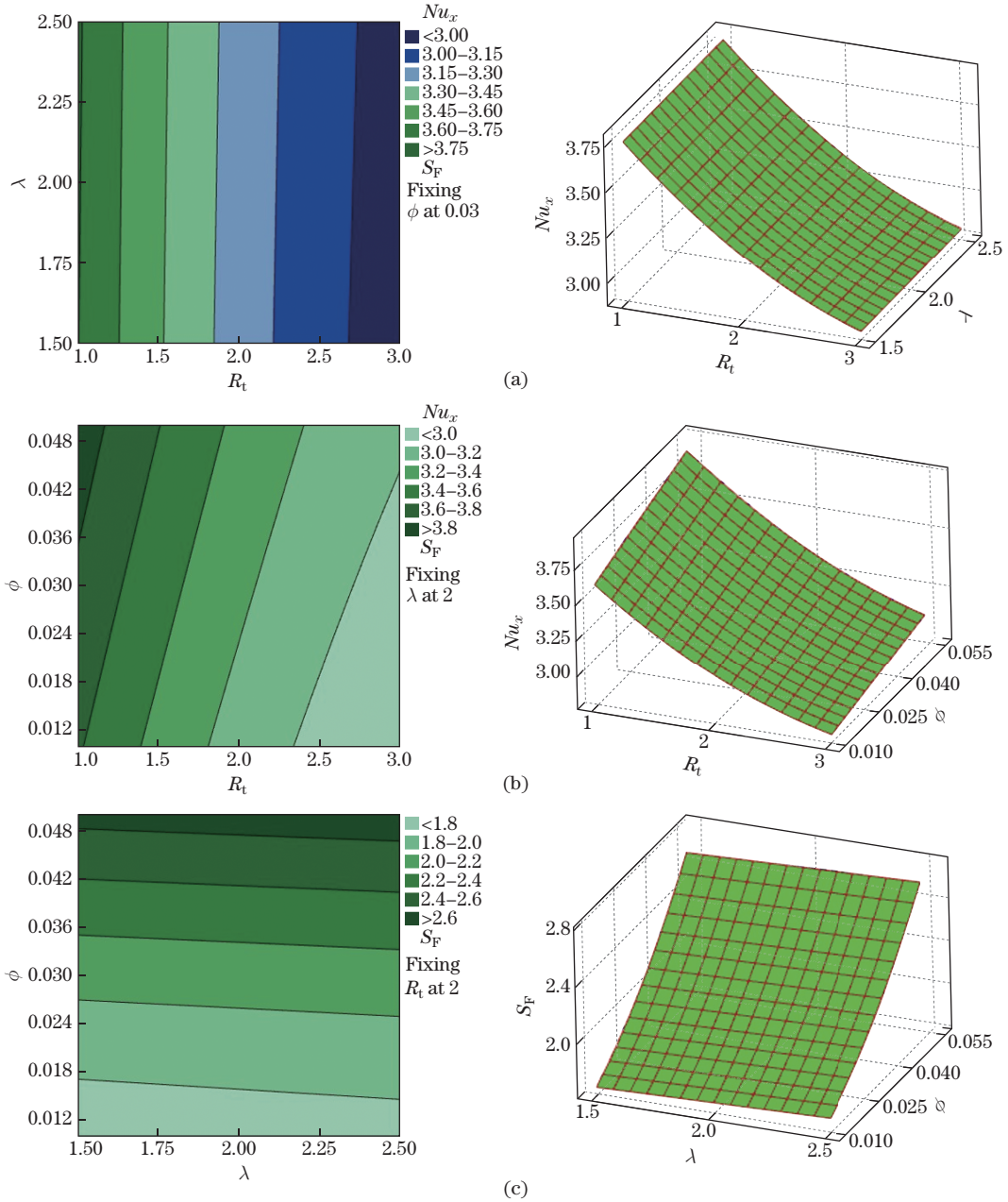

Fig. 12 Contour (left) and surface plots (right) for Nu_x (color online)

on Nu_x. The maximum heat transport is noticed when λ and ϕ are kept at a high level.

4.3 sensitivity analysis

The sensitivities of S_F and Nu_x towards R_t, λ, and ϕ are evaluated via the following sensitivity functions:

$$\begin{cases} \dfrac{\partial S_F}{\partial R_t} = 0.021\ 412 - 0.004\ 082 R_t + 0.005\ 229\lambda + 0.002\ 637\phi, \\ \dfrac{\partial S_F}{\lambda} = 0.023\ 601 + 0.005\ 229 R_t + 0.002\ 615\phi, \\ \dfrac{\partial S_f}{\partial \phi} = 0.495\ 628 + 0.208\ 164\phi + 0.002\ 637 R_t + 0.002\ 615\lambda, \end{cases} \tag{19}$$

$$\begin{cases} \dfrac{\partial Nu_x}{\partial R_{\mathrm{t}}} = -0.418\ 60 + 0.214\ 96R_{\mathrm{t}}, \\ \dfrac{\partial Nu_x}{\partial \lambda} = 0.006\ 94, \\ \dfrac{\partial Nu_x}{\partial \phi} = 0.120\ 52 - 0.023\ 43R_{\mathrm{t}}. \end{cases} \tag{20}$$

The sensitivity of S_{F} and Nu_x for different values of R_{t} and ϕ by fixing λ at the middle level is illustrated in Figs. 13–14. Here, the positive and negative bar chart indicates the increment and decrement in S_{F} and Nu_x, correspondingly. The greater the height of the bar, the more sensitive the response will be toward the variable.

From Fig. 13, the sensitivities of S_{F} towards R_{t}, λ, and ϕ are found to be positive at all levels of ϕ by passing R_{t} from -1 to $+1$. Also, it is noticed that the sensitivity of S_{F} to ϕ is highest at high levels of R_{t} and ϕ, and enhances with an increase in ϕ and R_{t}. The sensitivity of S_{F} to λ increases with ϕ by passing R_{t} from -1 to $+1$. The sensitivity of S_{F} to R_{t} decays and advances with R_{t} and ϕ respectively. However, S_{F} is more sensitive to ϕ compared with R_{t} and λ, specifically in the high levels of R_{t} and ϕ.

The sensitivities of Nu_x towards R_{t}, λ, and ϕ are displayed in Fig. 14. Since the sensitivity of Nu_x to λ and ϕ is always positive, Nu_x increases with the increase in λ and ϕ. Focusing on the sensitivity of N_x to λ, no change is noticed when R_{t} and ϕ changes from level -1 to $+1$. The sensitivity of Nu_x to R_{t} is always negative and hence R_{t} has a decreasing impact on Nu_x. Also, no change is noticed when ϕ changes from level -1 to $+1$. The sensitivity of Nu_x to ϕ decreases when R_{t} changes from -1 to $+1$. The Nusselt number is more sensitive to R_{t} than λ and ϕ.

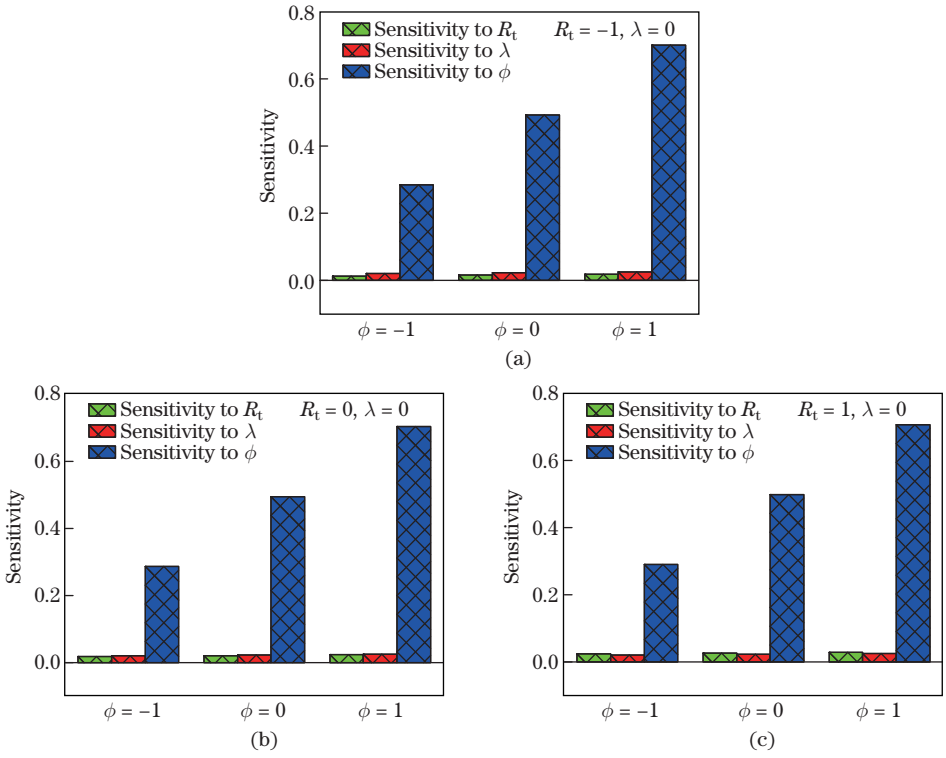

Fig. 13 Sensitivity analysis for S_{F} when $\lambda = 0$ (color online)

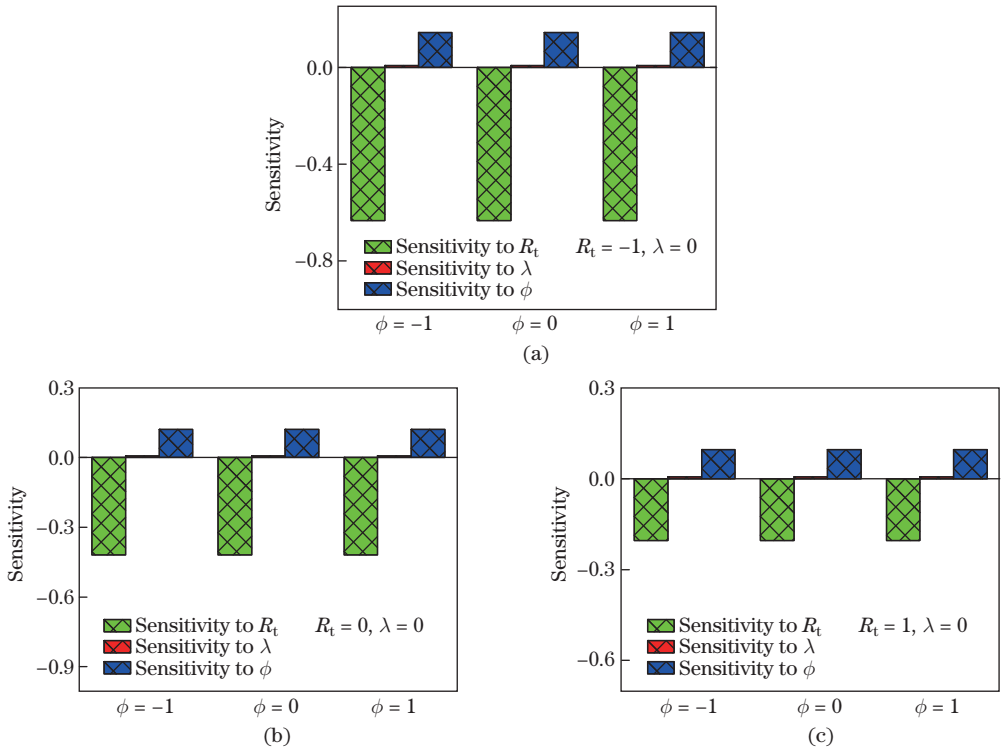

Fig. 14 Sensitivity analysis for Nu_x when $\lambda = 0$ (color online)

5 Conclusions

The results obtained from the analysis are summarized as follows.

(i) The velocity profile decays due to the NP aggregation.

(ii) The temperature field is found higher in the presence of NP aggregation.

(iii) The velocity and temperature fields are positively related to the radiation aspect.

(iv) The heat transport increases due to the curvature of the cylinder.

(v) The friction factor is more sensitive to NP volume fraction compared with the radiation aspect and mixed convection aspect.

(vi) The Nusselt number is more sensitive to thermal radiation aspect than mixed convection and NPs volume fraction.

Acknowledgements The authors are grateful to the management of CHRIST (Deemed to be University), India, for their support through the major research project (MRP). The authors also thank the editors and reviewers for their constructive suggestions on the manuscript.

References

[1] CHOI, S. U. and EASTMAN, J. A. Enhancing thermal conductivity of fluids with nanoparticles. *Proceedings of the ASME International Mechanical Engineering Congress and Exposition*, **66**, 99–105 (1995)

[2] HOSSEINZADEH, K., AFSHARPANAH, F., ZAMANI, S., GHOLINIA, M., and GANJI, D. D. A numerical investigation on ethylene glycol-titanium dioxide nanofluid convective flow over a

stretching sheet in presence of heat generation/absorption. *Case Studies in Thermal Engineering*, **12**, 228–236 (2018)

[3] MAHANTHESH, B., LORENZINI, G., OUDINA, F. M., and ANIMASAUN, I. L. Significance of exponential space and thermal-dependent heat source effects on nanofluid flow due to radially elongated disk with Coriolis and Lorentz forces. *Journal of Thermal Analysis and Calorimetry*, **141**, 37–44 (2020)

[4] MEBAREK-OUDINA, F. Convective heat transfer of titania nanofluids of different base fluids in cylindrical annulus with discrete heat source. *Heat Transfer—Asian Research*, **48**(1), 135–147 (2019)

[5] ROŞCA, N. C., ROŞCA, A. V., POP, I., and MERKIN, J. H. Nanofluid flow by a permeable stretching/shrinking cylinder. *Heat and Mass Transfer*, **56**(2), 547–557 (2020)

[6] CHEN, H., DING, Y., HE, Y., and TAN, C. Rheological behaviour of ethylene glycol based titania nanofluids. *Chemical Physics Letters*, **444** (4-6), 333–337 (2007)

[7] CHEN, H., WITHARANA, S., JIN, Y., KIM, C., and DING, Y. Predicting thermal conductivity of liquid suspensions of nanoparticles (nanofluids) based on rheology. *Particuology*, **7**(2), 151–157 (2009)

[8] ELLAHI, R., HASSAN, M., and ZEESHAN, A. Aggregation effects on water base Al_2O_3-nanofluid over permeable wedge in mixed convection. *Asia-Pacific Journal of Chemical Engineering*, **11**(2), 179–186 (2016)

[9] BENOS, L. T., KARVELAS, E. G., and SARRIS, I. E. Crucial effect of aggregations in CNT-water nanofluid magnetohydrodynamic natural convection. *Thermal Science and Engineering Progress*, **11**, 263–271 (2019)

[10] ACHARYA, N., DAS, K., and KUNDU, P. K. Effects of aggregation kinetics on nanoscale colloidal solution inside a rotating channel. *Journal of Thermal Analysis and Calorimetry*, **138**(1), 461–477 (2019)

[11] MUKHOPADHYAY, S. and ISHAK, A. Mixed convection flow along a stretching cylinder in a thermally stratified medium. *Journal of Applied Mathematics*, **2012**, 491695 (2012)

[12] MAHANTHESH, B., GIREESHA, B. J., GORLA, R. R., ABBASI, F. M., and SHEHZAD, S. A. Numerical solutions for magnetohydrodynamic flow of nanofluid over a bidirectional non-linear stretching surface with prescribed surface heat flux boundary. *Journal of Magnetism and Magnetic Materials*, **417**, 189–196 (2016)

[13] HAYAT, T., QAYYUM, S., ALSAEDI, A., and ASGHAR, S. Radiation effects on the mixed convection flow induced by an inclined stretching cylinder with non-uniform heat source/sink. *PLoS One*, **12**(4), e0175584 (2017)

[14] PANDEY, A. K. and KUMAR, M. Natural convection and thermal radiation influence on nanofluid flow over a stretching cylinder in a porous medium with viscous dissipation. *Alexandria Engineering Journal*, **56**(1), 55–62 (2017)

[15] SHIT, G. C. and MUKHERJEE, S. MHD graphene-polydimethylsiloxane Maxwell nanofluid flow in a squeezing channel with thermal radiation effects. *Applied Mathematics and Mechanics* (*English Edition*), **40**(9), 1269–1284 (2019) https://doi.org/10.1007/s10483-019-2517-9

[16] MAHMOOD, T. and MERKIN, J. H. Similarity solutions in axisymmetric mixed-convection boundary-layer flow. *Journal of Engineering Mathematics*, **22**(1), 73–92 (1988)

[17] ISHAK, A. Mixed convection boundary layer flow over a vertical cylinder with prescribed surface heat flux. *Journal of Physics A*: *Mathematical and Theoretical*, **42**(19), 195501 (2009)

[18] RAMACHANDRAN, N., CHEN, T. S., and ARMALY, B. F. Mixed convection in stagnation flows adjacent to vertical surfaces. *ASME Journal of Heat Transfer*, **110**(2), 373–377 (1988)

[19] MABOOD, F., LORENZINI, G., POCHAI, N., and IBRAHIM, S. M. Effects of prescribed heat flux and transpiration on MHD axisymmetric flow impinging on stretching cylinder. *Continuum Mechanics and Thermodynamics*, **28**(6), 1925–1932 (2016)